Editors' Suggestion

Mechanosensing Potentials Gate Fuel Consumption in a Bipedal DNA Nanowalker

Shern Ren Tee, Xinpeng Hu, Iong Ying Loh, and Zhisong Wang*
Department of Physics, National University of Singapore, 2 Science Drive 3, Singapore 117542, Singapore

(Received 17 October 2017; revised manuscript received 27 February 2018; published 26 March 2018; corrected 26 March 2018)

A bipedal DNA nanowalker was recently reported to convert chemical energy into directional motion autonomously and efficiently. To elucidate its chemomechanical coupling mechanisms, three-dimensional molecular modeling is used to obtain coarse-grained foot-track binding potentials of the DNA nanowalker via unbiased and biased sampling techniques (for the potentials' basin and high-energy edges, respectively). The binding state that is protected against fuel-induced dissociation responds asymmetrically to forward versus backward forces, unlike the unprotected state, demonstrating a mechanosensing capability to gate fuel binding. Despite complex DNA mechanics, the foot-track potential exhibits a surprisingly neat three-part profile, offering some general guidelines to rationally design efficient nanowalkers. Subsequent modeling of the bipedal walker attached to the track gives estimates of the free energy for each bipedal state, showing how the mechanosensing foot-track binding breaks the symmetry between the rear and front feet, enabling the rear foot to be selectively dissociated by fuel and generating efficient chemomechanical coupling.

DOI: 10.1103/PhysRevApplied.9.034025

I. INTRODUCTION

A bipedal DNA nanowalker was recently reported to convert chemical energy into directional motion autonomously and efficiently [1], using identical feet to walk along periodically spaced binding sites on a linear track like natural biomolecular nanowalkers. DNA fuel molecules dislodge the rear foot by displacement and are then cleaved by an endonuclease, regenerating the foot which subsequently rebinds to the track. The DNA nanowalker thus converts the chemical energy of fuel strands into mechanical motion, analogous to the adenosine triphosphate (ATP)-fueled motion of biomolecular nanowalkers. This autonomous DNA walker is among the several reported artificial nanowalkers [1–5] that go beyond the previous burning-bridge designs [6–14].

Such an efficient nanowalker requires the chemical cycle of fuel hydrolysis to be mechanically gated at each walker foot, according to its position and binding state. Specifically, the fuel cycle should dissociate the trailing (or rear) foot instead of the leading (or front) foot, giving a selective dissociation bias. The dissociated foot should rebind forward rather than backward, or closer to the plus end of the track instead of the minus end, giving a forward binding bias. Both biases are required for a good walker [15,16]. While thermodynamics imposes an upper limit to the total directionality achievable by fuel energy input [17], actually achieving that upper limit requires intricate mechanisms to enable mechanical gating of fuel consumption, yet to be fully elucidated for natural or artificial nanowalkers.

One major contribution comes from the role of intramolecular strain, which is known to contribute to the interfoot coordination of kinesin stepping [18] and artificial nanowalkers [19]. When a nanowalker is bound with both feet to the track, intramolecular strain mechanically distinguishes a front foot, which is strained backward, from a rear foot, which is instead strained forward. A *mechanosensing* foot-track binding, which displays differing chemical affinities for a substrate in response to mechanical strain, then provides a substrate-based dissociation bias. Kinesin indeed exhibits such chemomechanical coupling, with internal strain capable of blocking ATP from binding to the leading motor head [20], contributing to selective dissociation.

Motor proteins can thus shed light on molecular mechanisms for mechanosensing and efficient chemomechanical coupling. However, it can be difficult to reverse engineer their evolutionarily optimized designs, and direct observation of their rapid motion and efficient fuel consumption pushes single-molecule techniques to their limits. By contrast, a rapidly expanding family of DNA nanomotors [1,3,4,21] allow for design hypotheses to be rationally and incrementally implemented, modified, and tested.

The walker of Ref. [1] displays autonomous, processive, and directional fuel-driven motion, owing in part to selective dissociation derived from mechanosensing foot-track binding. The walker (Fig. 1) is annealed from two

*phywangz@nus.edu.sg

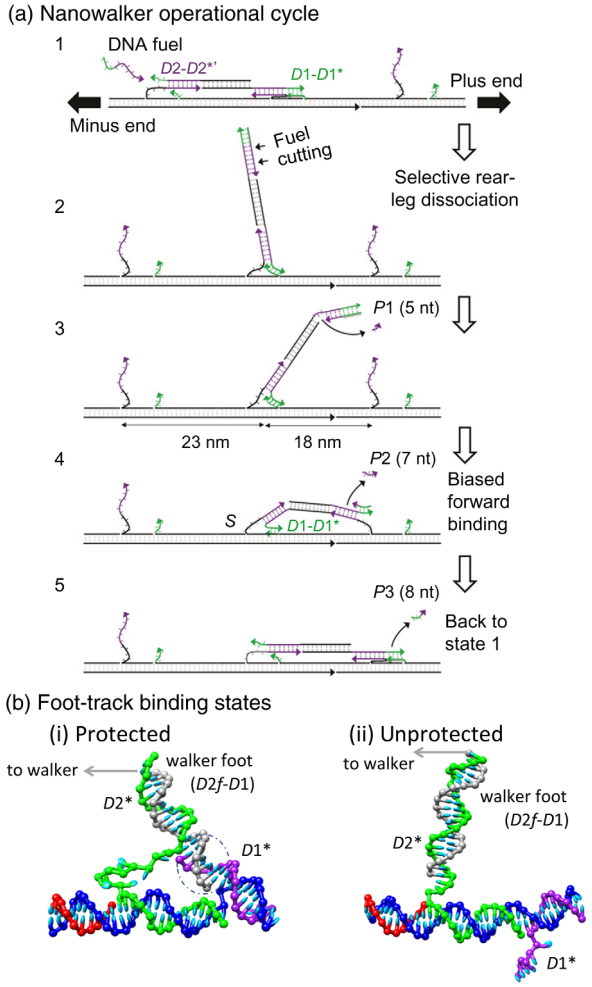

FIG. 1. *DNA nanowalker walking cycle and foot-track binding.* (a) The nanowalker walking cycle includes a strong preference, or bias, for fuel to dissociate the rear foot instead of the front foot of a walker bipedally bound to the track. (b) This dissociation bias occurs because the foot can bind to the track in one of two configurations: the foot (silver) is either protected, by means of attachment both to the short overhang $D1*$ (purple) and the long overhang $D2*$ (green), or unprotected, with the detachment of $D1*$ leaving mismatches between the walker leg and the overhang $D2*$ which can be attacked by a single-stranded fuel molecule. (All DNA configurations are modeled using oxDNA2 [22] and visualized using UCSF Chimera [23]; the track is oriented with the plus end or forward direction towards the right.)

40-nucleotide (nt) strands to form a 20-base-pair (bp) walker body, capped on either side with 20-nt single-stranded DNA, these strands forming the legs of the nanowalker. The track contains equally spaced binding sites, with each binding site containing a short 6-nt overhang (labeled $D1*$) and a long 14-nt overhang (labeled $D2*$) atop a 9-nt tether for binding flexibility, which bind via Watson-Crick complementarity to the nanowalker's feet. Experiments show that when both feet of the walker are bound to the track, fuel predominantly dissociates the rear foot instead of the front foot, contributing a selective dissociation bias towards its directional motion.

The proposed explanation [1] is that forward strain destabilizes the $D1*$ short helix by significantly curving it, exposing the rear but not the front foot to fuel-induced displacement. That is, forward strain causes the foot-track binding to exhibit an *unprotected* configuration, allowing fuel to invade at the exposed $D1$ segment of the walker foot, while backward strain enables a *protected* configuration which instead rejects fuel invasion [Fig. 1(b)], giving rise to a selective dissociation bias.

We note in passing that, without chemical energy input, detailed balance ensures that the walker will not exhibit any directional motion, on average, despite displaying selective dissociation. Specifically, the selectively dissociated rear foot would preferentially reattach to the rear binding site that it just left. Thus, a nicking enzyme N.BbvC IB is supplied to use chemical energy (from excess ATP in solution) to cut the foot-bound fuel. The fuel fragment dissociation supplies an additional forward binding bias by ensuring that the binding transitional state is different from the dissociation transitional state, at the cost of externally supplied chemical energy (see Ref. [1] for further details of this forward bias), and the released chemical energy powers the walker's directional motion. Without downplaying the importance of this binding bias, the remainder of this paper focuses on the selective dissociation bias, and how it can be examined via studying the foot-track binding assembly and its mechanosensing capabilities, first as an isolated system and then as the components of a full bipedal nanowalker.

Thus, the structure and the function of rationally designed DNA nanowalkers are potentially easier to elucidate than for nature-derived motor proteins. The base-pairing and stacking interactions of DNA are also easier to model than the sophisticated interactions and conformational changes of protein structures, allowing for an easier prediction and simulation of mechanical structures. This work demonstrates such methods using the computationally efficient three-dimensional molecular simulation package oxDNA2 [22].

II. OBTAINING FOOT-TRACK BINDING POTENTIALS IN PROTECTED AND UNPROTECTED STATES

A. Simulation methods for foot-track binding

oxDNA2 is first used to simulate the foot-track binding complex in the protected or the unprotected state, to obtain a suitable coarse-graining coordinate and an effective potential in that coordinate for either state, using sequences from Sec. A 1. The simulation system comprises the 20-nt foot, the two track overhangs and the 15-bp segment between them, and 10 bp of additional track on either side to avoid spurious contributions from terminal stacking interactions, as shown in Fig. 1(b). Virtual-move Monte Carlo (MC) sampling is then conducted at a temperature of 27 °C and an effective salt

concentration of $1.0M$. At various values of imposed force from 20 pN backward to 20 pN forward (including zero force), over simulations totaling 10^8 MC sweeps, configurations are recorded every 50 sweeps (to avoid correlation effects) to give 10^5 data points. When the loading force is nonzero, it is imposed on the last nucleotide of the motor foot, as shown in Fig. 3(a). Harmonic traps (which exert a restoring force on a given nucleotide proportional to its displacement from a chosen point) are additionally imposed on the nucleotides at either end of the track to maintain the position and orientation of the assembly. When the loading force is zero, the harmonic traps are also removed to provide simulations of the system under no external constraints.

Each recorded configuration (for protected and unprotected states alike) is then coarse grained by calculating the vectors $\mathbf{r}_{\text{track}}$ from the minus end to the plus end of the track segment and $\mathbf{r}_{\text{motor}}$ from the minus end of the track segment to the terminal nucleotide of the motor foot, as shown in Fig. 3. The displacement coordinate, $x \equiv \left(\mathbf{r}_{\text{motor}} \cdot \mathbf{r}_{\text{track}} / \mathbf{r}_{\text{track}} \cdot \mathbf{r}_{\text{track}} - \frac{1}{2}\right) |\mathbf{r}_{\text{track}}|$, then measures the distance between the midpoint of $\mathbf{r}_{\text{track}}$ and $\mathbf{r}_{\text{motor}}$ projected along $\mathbf{r}_{\text{track}}$. Sorting x into bins 0.2 nm wide then yields the probability distribution of x under loading force F, which we label $\Pr_1^F(x)$ for the protected state and $\Pr_0^F(x)$ for the unprotected state.

In turn, by the Boltzmann distribution formula $\beta\phi(x) = -\ln \Pr(x)$ (where $\beta \equiv 1/k_B T$ is the inverse normalized temperature), each probability distribution of x gives an effective potential for x under force F, which we label $\phi_1^F(x)$ for the protected state and $\phi_0^F(x)$ for the unprotected state. These biased potential landscapes are analogous to the (unweighted) results of umbrella sampling [24], but in this case, the biasing force does not act directly on the coarse-grained displacement x. Nonetheless, the potentials $\phi_1^F(x)$ and $\phi_0^F(x)$ can each be debiased by approximating F as a constant force in x to yield an estimate of the unbiased potentials: $\phi_1(x)$ [or $\phi_0(x)$] $\approx \phi_1^F(x) - Fx$ [or $\phi_0^F(x) - Fx$] to within an additive constant. This approximation is surprisingly robust and yields consistent landscapes up to $15 k_B T$ from the minimum energy, with the discrepancies between overlapping simulations mostly within $0.5 k_B T$, as seen in Fig. 2(b).

As with umbrella sampling, therefore, biased simulations from a wide range of loading forces can be combined to estimate the potential landscapes for the protected and unprotected states, allowing in particular the measurement of high-free-energy regions which would be very rarely visited in an unbiased simulation. These estimates can be compared directly with the results of unbiased simulations, which omit all external forces. As shown in Fig. 2(c), when the harmonic traps are 10.2 nm apart, the estimated potentials are consistent with the results of unbiased simulations, while smaller or larger distances introduce discrepancies. The potential profiles obtained under that

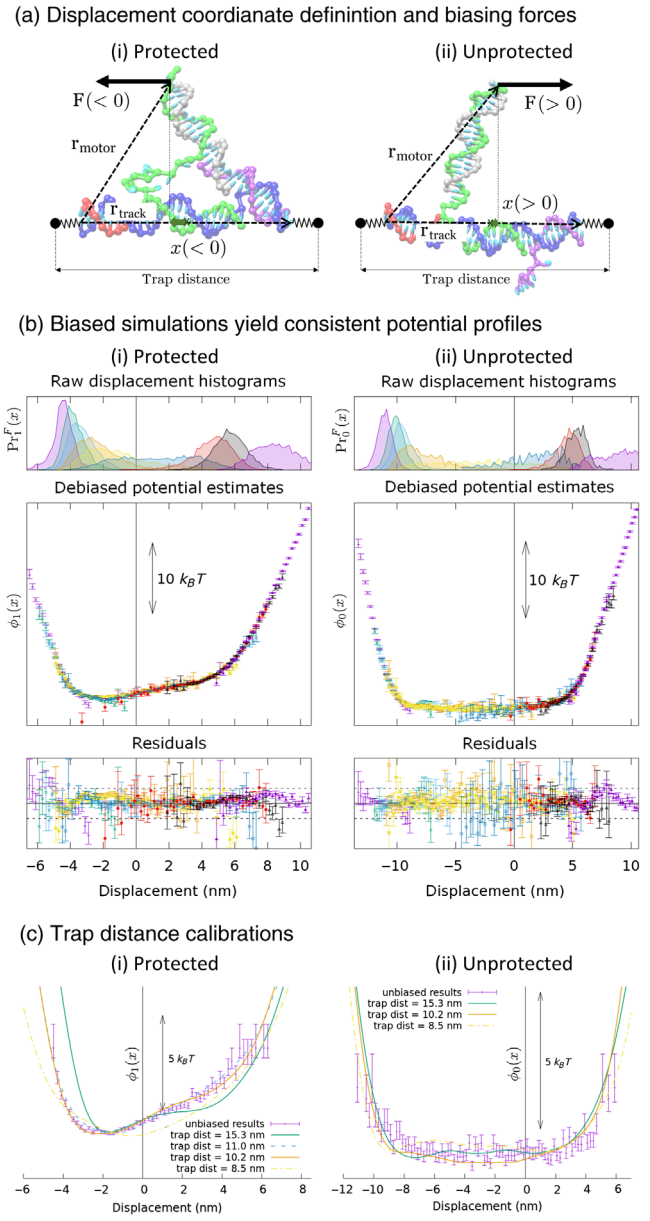

FIG. 2. *Measuring the foot-track potential landscape via simulation.* (a) The foot displacement is measured relative to the track center using vectors $\mathbf{r}_{\text{motor}}$ and $\mathbf{r}_{\text{track}}$, creating a position coordinate x; for biased simulations, a biasing force $\mathbf{F}$ is applied to the motor foot while harmonic traps at either end of the track assembly (illustrated with spring symbols) localize the system. (b) (Top panels) x distributions are obtained under forces of (from left to right for each graph) backward 20, 15, 10, 6, and 2 pN; 0 pN; and forward 2, 6, 10, 15, and 20 pN. (Middle panels) Debiased log probabilities overlap neatly, with aggregation and smoothing yielding the curves shown in Fig 3. (Bottom panels) Residuals, obtained by subtracting individual data points from the smoothed aggregate, are mostly within $\pm 0.5 k_B T$ (the dashed lines) and are larger only for more-uncertain points. (c) Different trap distances for the biased simulations give different aggregated landscapes; consistency with unbiased simulations is achieved for a trap distance of 10.2 nm.

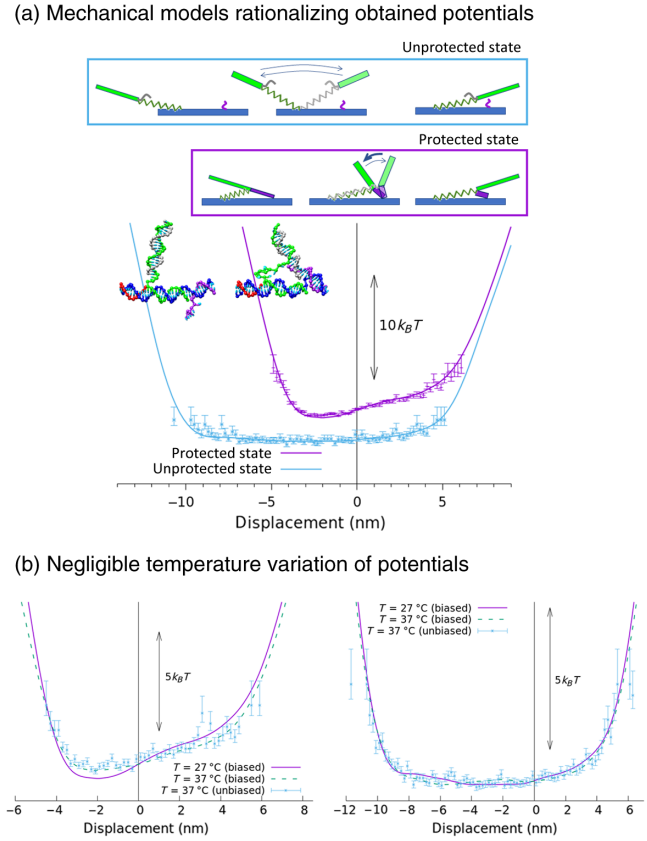

FIG. 3. *Rationalizing mechanosensing potential landscapes.* (a) Mechanical models (top panels) can qualitatively rationalize the potential landscapes (bottom panel) obtained for protected and unprotected states. In the unprotected state, at either margin, displacement can be increased only by imposing elastic strain, resulting in approximately quadratic edges; unimpeded angular diffusion between results in a flat, approximately linear middle region. The protected state has approximately quadratic edges similar to the unprotected state, but the middle region is no longer flat; angular diffusion is impeded by internal tension due to the free-energy costs of stretching the single-stranded tether and unstacking between long and short double helices, resulting in internal tension (shown schematically by the boldface arrow). (b) Increasing the temperature of the simulation from 27 °C to 37 °C results in negligible change.

trap distance are thus used to analyze the mechanosensing nature of the foot-track binding, as we now discuss.

B. Foot-track binding potentials obtained

As shown in Fig. 3, the potential landscapes for protected and unprotected states are noticeably different. The typical x range for the protected state is far forward of the range of the unprotected state, due to the additional constraint of the $D1*$ short overhang. Each landscape has a middle linear portion representing angular diffusion of the foot; on either side, the curvature then increases significantly, indicating the onset of elastic stretching. These landscapes can be modeled by a piecewise combination of quadratic and linear terms:

$$\phi(x) = \begin{cases} \frac{k_-}{2}(x - x_-)^2, & x \le x_- \\ f(x - x_-), & x_- < x \le x_+ , \\ \frac{k_+}{2}(x - x_+)^2 + f(x_+ - x_-), & x > x_+ \end{cases} \quad (1)$$

where the spring constants k_- and k_+ are determined by the curvatures of the left and right sides, respectively, the displacements x_- and x_+ estimate the boundaries between the left and right sides, respectively, and the middle region, and the intrinsic tension f is determined by the gradient of the middle region. This pattern can be explained qualitatively with reference to the simple mechanical models shown at the top of Fig. 3(a): the left and right sides are approximately quadratic because such large displacements require the elastic stretching of single- and double-stranded regions of DNA. The middle region is approximately linear because it involves angular diffusion; in the unprotected state, no significant stretching occurs and this region is flat, but in the protected state intrinsic tension exists due to the stretching of the single-stranded tether region and the unstacking between the long and short helices as x bends forward. Interestingly, increasing the simulation temperature from 27 °C to 37 °C results in negligible change to the obtained potential landscapes [Fig. 3(b)], consistent with material parameters such as persistence length remaining largely constant with temperature in the oxDNA2 model [22].

As seen in Table I, both states possess an asymmetry between the rear and front edges, but only the protected state has a significant intrinsic tension. In both states, the front spring constant, k_+, is smaller than the rear spring constant, k_-. It is unclear whether this asymmetry is physically inherent or depends on the choice of coordinates, especially given the large variation in peripheral curvature with trap distance seen in Fig. 2(c). Moreover, since this asymmetry exists in both states, it is unlikely to contribute to any mechanical distinction *between* states. However, there is intrinsic tension in the protected state that is absent from the unprotected state since f is about $0.4 k_B T/\text{nm}$, or 1.6 pN, for the protected potential, but zero for the unprotected potential, an asymmetry which persists under different trapping conditions. This value of f represents a rearward tension on the foot-walker joint exerted by the foot-track binding complex when the walker foot is protected. Equivalently, given a potential width of

TABLE I. *Fitting parameters for protected and unprotected potential landscapes*, using the functional form from Eq. (1).

Parameter	Protected	Unprotected
k_- (k_BT/nm^2)	2.42 ± 0.10	2.06 ± 0.16
x_- (nm)	-2.64 ± 0.06	-8.74 ± 0.08
f (k_BT/nm)	0.42 ± 0.02	0.018 ± 0.016
x_+ (nm)	3.50 ± 0.14	3.10 ± 0.05
k_+ (k_BT/nm^2)	1.09 ± 0.07	1.17 ± 0.10

$x_+ - x_- \approx 6$ nm, the intrinsic tension can be interpreted as imposing a mechanical energy penalty of about $2.4k_BT$ on a protected trailing foot as opposed to a protected leading foot, with all else being equal. This tension can thus serve a mechanosensing purpose, making fuel strands dissociate the rear foot more often than the front foot, leading to a selective dissociation bias, as experimentally observed.

III. MECHANOSENSING AND SELECTIVE BIAS IN FULL WALKER-TRACK BIPEDAL SIMULATIONS

The full system, consisting of the walker bipedally bound to the track, can be dissected into the following components: a rear and a front foot-track binding assembly, as well as two undecorated DNA double-helical domains for linkers, one of which serves as the *walker body* and one of which serves as the *track spacer*. The bipedally bound walker can occupy one of four states, which we label as follows, following the earlier convention of using 0 to denote an unprotected foot and 1 to denote a protected foot: 00 is the state in which both feet are unprotected, 01 (10) is the state in which the front (rear) foot is protected and the other foot is unprotected, and 11 is the state in which both feet are protected. The two states 01 and 10 are thus asymmetric, and in these states, the rear and the front foot, respectively, can be selectively dissociated by fuel; the ratio between these states thus directly determines whether dissociation is biased towards the rear or the front foot, while the symmetric states (00 and 11) influence only the overall speed and fuel efficiency of the walker.

Having identified mechanosensing behavior in the foot-track binding assembly, we now analyze simulations of the full system to see how this behavior enables selective dissociation bias in the bipedally bound walker, and how the magnitude of that bias varies with the lengths of the linkers.

A. Simulation methods for full walker-track systems

The full walker-track system is simulated with a 25-bp track spacer, giving the track an overall periodicity of 60 bp, and a walker body length which is varied from 15 to 35 bp in 5-bp increments, using the sequences listed in Sec. A 1. This track spacer length was used in experiments [1] together with a walker body length of 20 bp. Systems in each of the four states are simulated at a temperature of 27 °C and 1.0M salt, with graphics-processing-unit-accelerated Langevin molecular dynamics [25] used to speed up the simulations (given the absence of external force). For each walker body length and state, 10^8 simulation steps are used to yield 10^5 sample configurations.

As described earlier, each simulation configuration can be dissected into rear and front foot-track binding assemblies, and walker body and track spacer linkers. Thus, each simulation configuration is coarse grained into four scalar quantities. The rear displacement, x_r, and front displacement, x_f, are calculated by treating each foot-track binding assembly in isolation and determining the respective displacement coordinate, using the same methodology previously described. Meanwhile, the end-to-end distances of the walker body and the track spacer linkers are also recorded, as x_{wb} and x_{ts}, respectively.

Aggregating each of the four coarse-grained coordinates over all of the configurations obtained and binning into 0.2-nm bins thus gives four probability distributions for each walker body length and state (00, 01, 10, or 11): $\mathrm{Pr}_{\mathrm{biped}}(x_f)$, $\mathrm{Pr}_{\mathrm{biped}}(x_r)$, $\mathrm{Pr}_{\mathrm{biped}}(x_{\mathrm{wb}})$, and $\mathrm{Pr}_{\mathrm{biped}}(x_{\mathrm{ts}})$, which we label $\mathrm{Pr}_{\mathrm{biped}}(x_i)$ generically and refer to as the bipedal probability distributions for a given coarse-grained coordinate. Each bipedal probability distribution can, in turn, be visualized as an effective bipedal potential landscape $\phi_{\mathrm{biped}}(x_i)$, again following the Boltzmann distribution relation $\beta\phi_{\mathrm{biped}}(x_i) = -\ln \mathrm{Pr}_{\mathrm{biped}}(x_i)$. The bipedal potential landscapes give qualitative clues to the forces and constraints that relate the different components of the bipedal walker. These potential landscapes are shown in Fig. 4(b) for the four states for a walker body length of 20 bp; other walker body lengths show qualitatively similar results.

For the walker's feet, the bipedal potentials for the walker's feet are constrained first by the earlier-measured protected foot-track binding potential $\phi_1(x)$ or the unprotected foot-track binding potential $\phi_0(x)$. For the rear (front) foot, the bipedal potential follows the curved periphery of the single-foot potential at large positive (negative) x, with the dependence on the protected or unprotected state serving as further validation of the methods from Sec. II. However, as the rear (front) foot attempts to diffuse backward (forward), it becomes "bipedally constrained" due to intramolecular tension, and the bipedal potential obtained diverges from the foot-track binding potential. The gradients of these sections of each foot bipedal potential in Fig. 4 offer a rough estimation of the intramolecular tension to be on the order of 1–4 pN.

To similarly analyze the bipedal potentials for the walker body and track spacer, the free energy-extension curves $\phi_{\mathrm{dh}}(x)$ for DNA double helices under no loading force needed to be determined. These curves were obtained using umbrella sampling (details are given in the second section of the Appendix). Then, in the same way that the rear- and front-foot bipedal potentials can be compared to the foot-track binding potentials from Sec. II, the track spacer bipedal potential can be compared to the free energy-extension curve for a DNA double helix of 25 bp, and the walker body bipedal potential can be compared to the free energy-extension curve for a DNA double helix of 20 bp (in this particular system).

Doing this comparison for the walker body shows an extension in all states, as the mean extension is larger than the mean extension of the unperturbed free energy-extension curve. For the walker bridge length of 20 bp, this stress is larger when the front foot is protected (states 01 and 11),

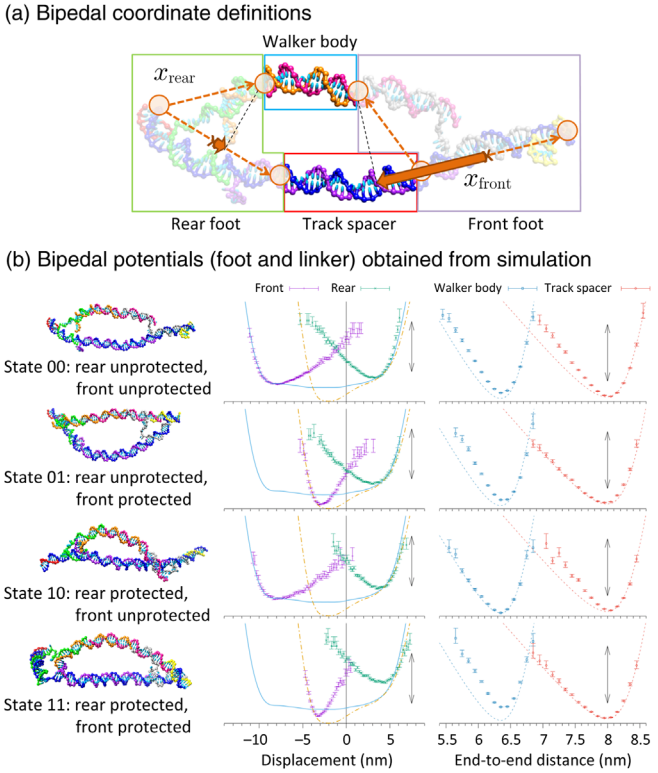

FIG. 4. *Componentwise analysis of bipedal configurations.* (a) Treating a bipedal configuration as a combination of two foot-track complexes joined by track and walker bridge strands, the single-leg equivalent displacement coordinates can be calculated at the front and rear of the bipedally attached motor. (b) The coordinate distributions yield effective potential landscapes for the front and rear feet in each of the four bipedal states (left column), here depicted for a bridge length of 20 base pairs. For each configuration, both front- and rear-foot effective potentials (data points, middle column) display self-constrained and bipedally constrained regions (where data points either fall on the lines or do not, respectively), with lines indicating the foot-track potentials obtained from Fig. 3. The walker body shows tension (particularly for states 01 and 11), while the track spacer is under tension for states 00 and 10 and in very minor contraction for states 01 and 11, as seen from comparing data points (right column) with dashed lines, which are energy-extension curves calculated from the parameters in Table II. All double-headed arrows denote $5k_BT$.

while the effect is smaller in the rear-foot protected states (10 and 11). The increase in stress is, in turn, consistent with the large displacement difference between the protected and the unprotected front foot—about 5 nm—compared to the near-zero displacement difference between the protected and the unprotected rear foot. Interestingly, the track spacer is also clearly under tension for front-unprotected states 00 and 10, while in front-protected states 01 and 11, the track spacer contracts, but only slightly. Some compensation between the walker body and track spacer can thus be observed, as the tension of the track spacer is largest when the walker body is least extended, and vice versa.

The mechanosensing foot-track binding thus reacts to the intramolecular tension of the walker body in two distinct ways. Since the walker body is shorter than the track spacer, intramolecular tension pulls rearward on the front foot. Given the large shift forward that protecting the front foot imposes, intramolecular tension should thus disfavor protecting the front foot, as reflected in the increased walker body tension seen in states 01 and 11. However, the intrinsic tension of the protected state imposes a penalty on protecting the rear instead of the front foot, as argued at the end of Sec. II. To compare these effects quantitatively, the total free energy of each bipedal state is calculated from the observed effective potentials of each coordinate, as described in the next section.

B. Estimating state free energies as a function of walker body length from coordinate distributions

The free energy of each bipedal state can be calculated from the free energies of the four components described above. For each component x_i, the empirical probability distribution $\mathrm{Pr}_{\mathrm{biped}}(x_i)$ can be used to calculate the component free energy $A_i \equiv \langle \phi_i \rangle - TS_i$. Here, $\langle \phi_i(x) \rangle$ is the ensemble average of the (unloaded) potential energy $\phi_i(x)$, which is just the single-foot potential $\phi_0(x)$ or $\phi_1(x)$ obtained in Sec. II for the front-foot (x_f) and rear-foot (x_r) displacement coordinates, and the free energy-extension curves $\phi_{\mathrm{dh}}(x)$ for the walker body and track spacer extensions, x_{wb} and x_{ts}; S_i is simply the usual Shannon entropy of the probability distribution $\mathrm{Pr}_{\mathrm{biped}}(x_i)$, and $T = 1$ to reflect that the free energy is being obtained at the same temperature as the simulation ensembles. Each potential $\phi_i(x)$ is offset to give zero free energy for the unperturbed distributions so that the obtained free energies represent the energetic cost of the constraints imposed by bipedal binding.

The resulting component energies for each state vary with walker body length, showing the effects of intramolecular tension. As shown in Fig. 5, the front- and rear-foot energies are predominantly controlled by their individual binding state. An unprotected rear foot has about $1k_BT$ surplus energy over an unprotected front foot—independent of whether the other foot is protected or not—while a protected rear foot has about $1.5k_BT$ surplus energy over a protected front foot. These energy differences persist whether we are comparing front and rear feet in symmetric states (for example, comparing the unprotected front- and rear-foot energies in state 00) or across asymmetric states (comparing the protected front-foot energy of state 01 to the protected rear-foot energy of state 10).

Indeed, the variation of the foot energy with walker body length also depends substantially on the binding state of the front foot. With an unprotected front foot (in either state 00 or state 10), foot energies decrease monotonically as the walker body length increases. By contrast, when the front foot is protected, foot energy increases with an increasing

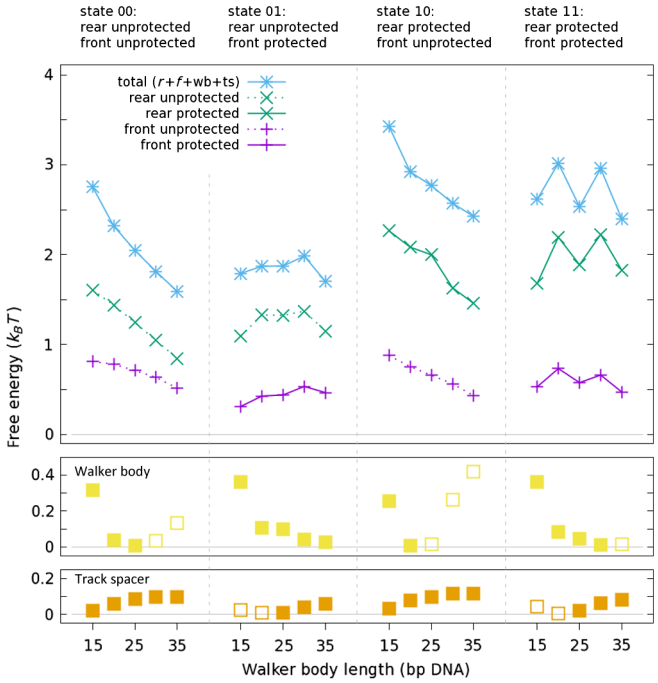

FIG. 5. *A breakdown of state free energies as a function of walker body length.* The free energy of each state as a function of walker body length can be estimated as a sum of the free energies of the rear foot, the front foot, the walker body, and the track spacer. All energies are calculated relative to the unbound configurations having zero free energy. Linker (walker body and track spacer) energies are shown at doubled vertical scale relative to the main plot, with filled symbols when the linker is under tension and empty symbols when the linker is under compression. 95% confidence intervals are the size of the symbols or smaller.

walker body length either weakly (state 01) or not at all (state 11). However, this pattern disappears when the front foot is protected. In state 01, when only the front foot is protected, foot and total energies are largely constant. In state 11, when both feet are protected, foot energies show irregular variation with walker body length. The free energies of the bound state show a pronounced periodicity of 10 bp in the walker length, especially in state 11.

The free energies of the walker body and the track spacer are small relative to the foot free energies, and also depend primarily on the binding state of the front foot. When the front foot is unprotected, walker body energy largely declines with increasing length, while track spacer energy is minimized around a walker body length of 20 bp. Conversely, when the front foot is protected, the walker body energy is minimized around a length of 25 bp, rising sharply with either a shorter or longer walker body, while track spacer energy is minimized at the shortest walker body length (15 bp) and rises with increasing length. However, these variations are much smaller than the changes in the foot free energies. Thus, the total free energy is dominated by the foot free energies and varies with walker body length in the same ways: the total free energy of front-unprotected states decreases sharply with an increasing walker body length, while the total free energy of front-protected states is influenced far less by walker body length and more, especially in the case of state 11, by the relative angle between ends of the walker body.

IV. DISCUSSION

A. Intramolecular tension creates a preference for the front-protected state

The data in Fig. 5 demonstrate how intramolecular tension creates a preference for the front-protected state. The walker body and track spacer energies are consistently small relative to the foot energies, showing that these segments are relatively flexible. The flexibility of these segments, in turn, reduces the free-energy cost expected from forward displacement against backward loading when protecting the front foot (noted as a possibility at the end of Sec. III A). As such, intramolecular tension predominantly reduces the free energy of a backward-loaded front-protected foot relative to a forward-loaded rear-protected foot, allowing the mechanosensing feet to coordinate a preference for protecting only the front foot.

The ability of the mechanosensing feet to gate fuel binding (and hence fuel consumption by the walker) is largely accounted for by the asymmetric three-slope pattern of the foot-track potential. Such a neat pattern for a real DNA walker is rather surprising considering the complex Watson-Crick base pairings responsible for the foot-track interaction. The three-slope pattern reminds us of simplistic sawtooth potentials that were widely used in previous theoretical studies of molecular motors. Therefore, the fuel-gating mechanism based on a three-slope mechanosensing potential found in this paper likely is generally applicable to the rational design of efficient fuel-powered nanowalkers. Previous modeling for artificial or biological nanowalkers [19,21,26–36] often depended on kinetic fitting or rough mechanical estimation from polymer theories. The surprisingly simple potential found using the realistic DNA simulation suggests the possibility of sequence-dependent kinetic-structural modeling for real DNA walkers based on potentials from sequence-dependent simulations.

The mechanosensing-based fuel gating is compatible with the size dependence of the total free energies for the walkers' bipedal states (Fig. 4). When the walkers' body length decreases from 35 to 15 bp, the asymmetric bipedal state (01) in which only the front leg is protected against fuel consumption remains low in free energy, but the other bipedal states rise. Such a size-dependent free-energy hierarchy is characteristic of a mechanics-mediated symmetry-breaking mechanism [19], which is identified in biological nanowalkers [26,27], as well as in artificial counterparts [21,28].

B. Predicting state populations and dissociation bias from state free-energy estimates

The free-energy cost of bipedal binding, over a hypothetical ensemble of the unbound components, is thus both measured from simulations and rationalized from considerations of a hypothetical cantilever coupling. Each such free energy is labeled A_{ij} for state ij, with a dependence on the walker body length that is left implicit. These measured free energies, in turn, relate to the free energy differences between states—specifically, given that the asymmetric states 01 and 10 consist of one protected foot and one unprotected foot, their free-energy difference can be calculated directly as the free-energy difference $A_{01} - A_{10}$. However, since the free energies of the symmetric states 00 and 11 are measured relative to different components (two unprotected feet and two protected feet, respectively), their free-energy differences must additionally include the free-energy cost of protecting instead of deprotecting a foot, which we label A_{prot}.

This additional free-energy difference A_{prot} cannot be accurately determined using the methods described in Secs. II and III, as they require a single simulation ensemble to repeatedly and reversibly sample the protected-unprotected transition. During both single foot and bipedal simulations, the protected state is repeatedly seen to transition to the unprotected state, but never vice versa, making it almost certain that the free energy of the unprotected state is less than that of the protected state, and thus that A_{prot} is positive. A positive value of A_{prot} can be rationalized as a large entropy penalty due to the "protecting" $D1*$ short overhang being far more localized in the protected state than in the unprotected state. Furthermore, some of the unprotected nucleotides on the walker foot are, in fact, adenosines, which are complementary to the thymines used in the tether, so that the deficit in hybridization free energy in the unprotected state is less than the theoretical six base pairs' worth.

Nonetheless, we can still calculate state free-energy differences and population occupancies as a function of A_{prot}. Taking the unknown free-energy cost of protection into account, the free energies of states 00, 01, 10, and 11 can be written, respectively, as $A_{00} - A_{\text{prot}}$, A_{01}, A_{10}, and $A_{11} + A_{\text{prot}}$, using the unbound components of either state 01 or 10 as the free-energy zero. As depicted in Fig. 6(b), the occupancies of the bipedal states are then simply Boltzmann distributed at thermal equilibrium.

A minimal model of foot dissociation shows how these population occupancies, in turn, set up a selective dissociation bias. Suppose an unprotected foot is dissociated by an incoming fuel molecule at some rate k_{off}, regardless of the positioning or force experienced, while a protected foot is never dissociated by an incoming fuel molecule. This means that intramolecular tension can affect only chemical rates via the mechanosensing protection state of either foot, not the chemical dynamics within each protection

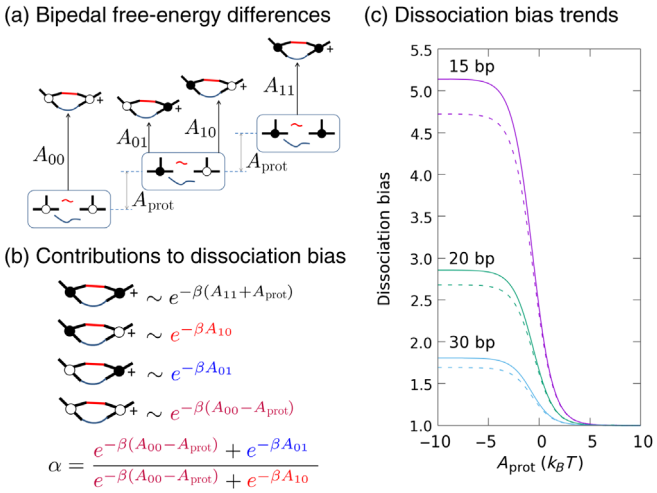

FIG. 6. *Estimating free energy differences, population occupancies and selective dissociation bias as a function of* A_{prot}. Estimating free-energy differences, population occupancies, and selective dissociation bias as a function of A_{prot}. (a) The state free energies A_{ij} are obtained relative to the unbound components possessing zero free energy. (b) Accounting for the unmeasured free energy of protection A_{prot}, each state is occupied in a Boltzmann distribution. Color coding shows how each state occupancy subsequently contributes to the selective dissociation bias α. (c) For a walker body length of 15, 20, or 30 bp at either 27 °C (the solid curves) or 37 °C (the dashed curves), the dissociation bias is plotted over $-10k_BT < A_{\text{prot}} < 10k_BT$.

state. Then state 00 contributes a rate proportional to $k_{\text{off}}e^{-\beta(A_{00}-A_{\text{prot}})}$ to dissociating either foot, while states 01 and 10 contribute dissociation rates proportional to $k_{\text{off}}e^{-\beta A_{01}}$ and $k_{\text{off}}e^{-\beta A_{10}}$ to rear- and front-foot dissociation, respectively. Now the selective dissociation bias α, defined as the ratio of rear-foot dissociation rates to front-foot dissociation rates, can then be calculated as

$$\alpha = \frac{e^{-\beta(A_{00}-A_{\text{prot}})} + e^{-\beta A_{01}}}{e^{-\beta(A_{00}-A_{\text{prot}})} + e^{-\beta A_{10}}} \tag{2}$$

in the regime where fuel-induced dissociation is much faster than rearrangement between the bipedal states. This expression tends towards 1 as $A_{\text{prot}} \to \infty$, as a strong chemical preference for unprotecting the foot favors state 00, and thus indiscriminate dissociation of both the front and rear feet by the fuel. When $A_{\text{prot}} \to -\infty$, on the other hand, α tends to its maximum value, $e^{\beta(A_{10}-A_{01})}$. In this regime, a strong chemical preference for protecting the foot favors state 11, a state in which no fuel-induced dissociation occurs. Then the overall speed of the walker decreases to near zero.

The resulting trends in dissociation bias against A_{prot} are plotted in Fig. 6(c), using the data displayed in Fig. 5. In addition to the bias at 27 °C, applying the formula $A = U - TS$ at a new temperature 37 °C allows the bias to be calculated at this new temperature as well. Given that

simulations show the foot-track binding potentials to be unchanged at 37 °C [Fig. 3(b)], this is the only adjustment needed to obtain the correct free energies at that temperature.

The selective dissociation bias in Eq. (2) corresponds to the walker's bias at saturated fuel concentration. For the walker with a 20-bp body length, the bias measured under this condition on short tracks (two or three binding sites) is between 1.1 and 2.5 [see Fig. 5(d) in Ref. [1]] at 25 °C, which is consistent with a A_{prot} between -1 and $2k_BT$. Further experiments [37] show this dissociation bias decreasing to around 1 at a higher temperature of 37 °C. A similar decrease of the dissociation bias from 25 °C to 37 °C is also observed [37] when the short binding overhang ($D1*$) is elongated from 6 to 10 nt and 14 nt. This work predicts an overall decrease of the bias with the temperature increase for the three walker body lengths (15, 20, and 30 bp) and over a wide range of A_{prot} values [from -10 to $10k_BT$; see Fig. 6(c)]. The predicted temperature dependence agrees with the experiments.

The bias change with temperature implies that βA_{prot} changes with temperature, and thus also that enthalpic and entropic contributions to A_{prot} have similar magnitudes at room temperature for this system, consistent with the contribution of both base-pairing energies and the entropic cost of confining the $D1*$ short overhang to the protection of the foot. Interestingly, biomolecular motors found in nature often display far less change in fuel efficiency with temperature. For example, the stall force of kinesin does not vary with temperature over its operating range [38], showing that the efficiency of its chemomechanical coupling remains constant. This temperature trend may indicate that part of effective biomimetic design will entail designing foot-track interactions that are largely entropic so that βA_{prot} does not change much with temperature.

Adjusting temperature is, in general, a practical way to optimize enzymatic nanomotors like the one studied in this paper since enzymes catalyzing chemical reactions of fuel molecules commonly exhibit a temperature-sensitive catalytic activity [2,39,40]. However, with the finding that bias decreases with an increasing temperature from 25 °C to 37 °C while the same temperature increase is known to increase the turnover rate of the nicking enzyme used for this DNA walker [2,40], understanding the overall effect of an increasing temperature (in particular, whether walker performance improves) turns out to involve a subtle balance between competing factors. Indeed, experimental operation of the DNA walker at 37 °C shows no apparent improvement [37] over the operation at 25 °C, which is consistent with the bias-temperature relation found for this walker.

V. CONCLUSION

Using a combination of unbiased and biased simulations, detailed energy profiles in this paper are measured for two possible binding states of the foot of an artificial nanowalker to its track binding site, in which it is either protected or unprotected against dissociation by fuel. These profiles reveal that the unprotected state has an essentially symmetrical response to forward and backward force, while the protected state incurs an energy penalty of about $2.4k_BT$ when loaded under forward force, as opposed to backward force. This mechanosensing behavior of foot-track binding is consistent with the experimentally measured high efficiency of this artificial nanowalker, implying an effective selective dissociation bias in which only the rear foot is dissociated by fuel interactions, not the front foot. They also match with earlier qualitative explanations that a short helix, responsible for protecting the walker foot against fuel dissociation, is unstable under forward loading due to high local curvature.

The foot-track binding energy profiles, together with energy profiles for the end-to-end extension of DNA double helices of various lengths, are then used to calculate free energies for the four possible states of a bipedally bound nanowalker, for different lengths of the walker body. The free energies of bipedal states indeed vary with walker body length, with different states having minimized inter-foot tension at different lengths, which is partially consistent with the presence of linker-controlled directionality effects. However, protecting the rear foot again consistently incurs an energy penalty of about $1.5k_BT$ relative to protecting the front foot, independent of the state of the other foot. The tension internal to the mechanosensing foot-track binding allows front-protected states to maintain a low total free energy even at short walker body lengths, while front-unprotected states with similar walker body lengths exhibit higher free energies and are thus less favored. Such internal tension provides a mechanism for generating a selective dissociation bias that is uniquely tolerant of, and even somewhat dependent on, the high flexibility of the linker portions, as seen in simulations.

With this selective dissociation mechanism, it is predicted that shortening the walker body from the experimentally tested value of 20 to 15 bp further enhances its selective dissociation bias, and thus its overall fuel efficiency; further shortening the walker body may well further enhance the system's effectiveness. More generally, one can imagine operating regimes for nanowalkers where internal and external tensions act in concert, rather than in opposition, on a mechanosensing foot-track binding. There is thus much room for improvement on the already-high efficiencies achieved by this system, and for the capabilities of artificial nanowalkers to further grow.

ACKNOWLEDGMENTS

All calculations were performed using high-performance computational resources at the Computer Centre and Graphene Research Centre of the National University of

Singapore. This work is supported by the Ministry of Education of Singapore under Grants No. R-144-000-320-112 and No. R-144-000-372-144 (to Z. W.).

APPENDIX: METHODS

1. Sequences

a. Foot-track binding

Track binding-site template: 5′-cap1-BS2-cap2-3′, cap1 = ACCTTCTGCT (10 nt), BS2 = GTGGCAGTTG TAGTC (15 nt), cap2 = CTGAACGAAA (10 nt).

Minus-end cap: 5′-cap1*-3′. (Asterisks denote complementary sequences.)

Long binding site: 5′-BS*-tether-$D2*$-3′, tether = TTTT TTTTT (9 nt), $D2*$ = C*T*TCAGCC*T*TCAGC (14 nt).

Plus-end cap and short binding site: 5′-cap2*-$D1*$-3′, $D1*$ = AGTTTA.

Walker foot: 5′-$D2f - D1$-3′, $D2f$ = GCTGA*G*GGCT GA*G*G (14 nt).

Assembly.—The 3′ and 5′ ends of the track binding-site template mark the plus and minus ends, respectively. The minus-end cap hybridizes to the 5′ minus end of the template, while the strand containing the short binding site caps the 3′ plus end. The long binding-site strand hybridizes to the middle section of the template. The template together with minus-end cap and both binding-site strands forms a complete binding site, to which the walker foot can bind as described in the main text. Note that the foot contains a sequence $D2f$ that is not fully complementary to the long binding site $D2*$; two mismatches (italicized) are originally incorporated to disrupt the endonuclease recognition site to prevent cleavage of the track binding site, and they are retained here for faithful modeling.

b. Bipedal simulation

Track template: 5′-cap0-BS1-TS-BS2-cap2-3′, cap0 = CACTTACGGA (10 nt), BS1 = CGTGTTTGTGCATCC (15 nt), TS = ATCTGGATTCTCCTGTCAGTTAGCTTT GGTGGTGTACCTTCTGCT (45 nt).

Minus-end cap: 5′-cap0*-3′.

Minus-end long binding site: 5′-BS1*-tether-$D2*$-3′.

Track spacer (including the minus-end short binding site): 5′-TS*-$D1*$-3′.

Plus-end long binding site: 5′-BS2*-tether-$D2*$-3′.

Plus-end cap and short binding site: 5′-cap2*-$D1*$-3′.

Walker strand 1: 5′-WS$n - D2f$-$D1$-3′.

Walker strand 2: 5′-WS$n*$-$D2f$-$D1$-3′. Here, the motor strand sequence depends on the number of base pairs n forming the walker body:

WS15: ATCTAGGTAGAGGCC (15 nt)

WS20: TTACCATCTAGGTAGAGGCC (20 nt)

WS25: CGGAATGCATCGCTCAGTGTTGATC (25 nt)

WS30: GAGTTACCATCTAGGTAGAGGCCTCGTACA (30 nt)

WS35: GTACAGAGTTACCATCTAGGTAGAGGCCT CGTACA (35 nt).

Assembly.—As before, the 3′ and 5′ ends of the track template mark the plus and minus ends, respectively. The minus-end cap, the BS1 long binding site and the 3′ end of the track spacer hybridize near the 5′ end of the track to form the minus-end binding site. The track spacer strand hybridized to the middle of the track forms a 45-bp spacer helix. The plus-end long and short binding-site strands hybridize to the 3′ end of the track to form the plus-end site. The two 3′ end sequences of the walker strands hybridize, forming a walker body of n base pairs with two 20-nt single-stranded feet protruding to bind to the track sites.

2. Energy-extension curves for DNA double helices

Umbrella sampling is used to obtain the free-energy curves for the end-to-end extension of DNA double helices from 15 to 55 bp long at a resolution of 0.1–0.2 nm (for randomly generated sequences). The simulations are conducted with a salt concentration of $1M$ at 27 °C, but variations from this curve at $2M$ salt and 37 °C are minimal. Within an energy range of about $10k_BT$ from the minimum, the energy curves can be empirically fitted with the following function:

$$E(x) = \frac{(f_+ - f_-)}{2}(x - x_0) + \frac{(f_+ + f_-)}{2}\sqrt{(x - x_0)^2 + d^2}, \quad f_+, f_-, d > 0 \tag{A1}$$

This expression tends towards linear functions $\pm f_\pm(x - x_0)$ as $x - x_0 \to \pm\infty$ (representing constant force), with an "elbow" around $x = x_0$ whose curvature is determined by d (representing an approximately harmonic potential about the contour length equal to about x_0).

The coefficients obtained by regression from individual curves are shown in Table II. They can, in turn, be generalized within the range 15–45 bp by simple regression on the number of nucleotides n, giving the unified expressions

TABLE II. *Energy-extension coefficients for DNA double helices from 15 to 55 bp.* 95% confidence intervals are given as uncertainties.

Length (bp)	f_- (k_BT/nm)	f_+ (k_BT/nm)	d (nm)	x_0 (nm)
15	17.1 ± 0.8	41.2 ± 5.0	0.29 ± 0.06	4.77 ± 0.06
20	10.3 ± 0.4	41.3 ± 4.0	0.32 ± 0.06	6.59 ± 0.06
25	6.5 ± 0.4	30.3 ± 2.0	0.35 ± 0.06	8.23 ± 0.06
30	4.8 ± 0.15	32.4 ± 2.0	0.31 ± 0.06	9.98 ± 0.06
35	3.52 ± 0.06	28.2 ± 1.0	0.34 ± 0.06	11.66 ± 0.06
45	2.15 ± 0.09	27.2 ± 1.0	0.39 ± 0.06	15.09 ± 0.06
55	1.58 ± 0.03	31.7 ± 1.0	0.55 ± 0.06	18.64 ± 0.06

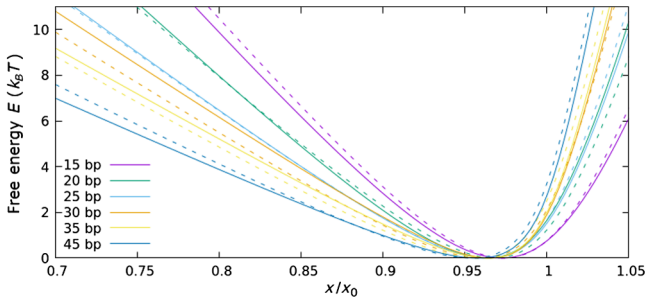

FIG. 7. *Energy-relative extension curves for DNA double helices of specified lengths, from 15 to 45 bp (top to bottom).* Solid lines use the coefficients in Table II, while dashed lines use the regressed coefficients from Eq. (A2). A relative extension (scaled against x_0) is used for ease of presentation.

$$x_0(n) = 0.345n - 0.377,$$
$$d(x_0) = 0.194 + 0.0159x_0,$$
$$f_+(x_0) = 28.0 + \frac{344}{x_0^2}, f_-(x_0) = 0.727 + \frac{385}{x_0^2}. \quad \text{(A2)}$$

As shown in Fig. 7, energy profiles using the regressed expressions (the dashed lines) approximate the individual energy profiles (the solid lines) closely enough for practical use.

[1] M. Liu, J. Cheng, S. R. Tee, S. Sreelatha, I. Y. Loh, and Z. Wang, Biomimetic autonomous enzymatic nanowalker of high fuel efficiency, ACS Nano **10**, 5882 (2016).

[2] J. Bath, S. J. Green, K. E. Allen, and A. J. Turberfield, Mechanism for a directional, processive, and reversible DNA motor, Small **5**, 1513 (2009).

[3] J. Cheng, S. Sreelatha, R. Hou, A. Efremov, R. Liu, J. R. C. van der Maarel, and Z. Wang, Bipedal Nanowalker by Pure Physical Mechanisms, Phys. Rev. Lett. **109**, 238104 (2012).

[4] I. Y. Loh, J. Cheng, S. R. Tee, A. Efremov, and Z. Wang, From bistate molecular switches to self-directed track-walking nanomotors, ACS Nano **8**, 10293 (2014).

[5] Q. Y. Yeo, I. Y. Loh, S. R. Tee, Y. H. Chiang, J. Cheng, M. H. Liu, and Z. S. Wang, A DNA bipedal nanowalker with a piston-like expulsion stroke, Nanoscale **9**, 12142 (2017).

[6] W. B. Sherman and N. C. Seeman, A precisely controlled DNA biped walking device, Nano Lett. **4**, 1203 (2004).

[7] J.-S. Shin and N. A. Pierce, A synthetic DNA walker for molecular transport, J. Am. Chem. Soc. **126**, 10834 (2004).

[8] P. Yin, H. Yan, X. G. Daniell, A. J. Turberfield, and J. H. Reif, A unidirectional DNA walker that moves autonomously along a track, Angew. Chem., Int. Ed. Engl. **43**, 4906 (2004).

[9] J. Bath, S. J. Green, and A. J. Turberfield, A free-running DNA motor powered by a nicking enzyme, Angew. Chem., Int. Ed. Engl. **44**, 4358 (2005).

[10] Y. Tian, Y. He, Y. Chen, P. Yin, and C. Mao, A DNAzyme that walks processively and autonomously along a one-dimensional track, Angew. Chem., Int. Ed. Engl. **44**, 4355 (2005).

[11] T. Omabegho, R. Sha, and N. C. Seeman, A bipedal DNA Brownian motor with coordinated legs, Science **324**, 67 (2009).

[12] M. von Delius, E. M. Geertsema, and D. A. Leigh, A synthetic small molecule that can walk down a track, Nat. Chem. **2**, 96 (2010).

[13] K. Lund, A. J. Manzo, N. Dabby, N. Michelotti, A. Johnson-Buck, J. Nangreave, S. Taylor, R. Pei, M. N. Stojanovic, N. G. Walter, E. Winfree, and H. Yan, Molecular robots guided by prescriptive landscapes, Nature (London) **465**, 206 (2010).

[14] Y. He and D. R. Liu, Autonomous multistep organic synthesis in a single isothermal solution mediated by a DNA walker, Nat. Nanotechnol. **5**, 778 (2010).

[15] A. Efremov and Z. Wang, Maximum directionality and systematic classification of molecular motors, Phys. Chem. Chem. Phys. **13**, 5159 (2011).

[16] A. Efremov and Z. Wang, Universal optimal working cycles of molecular motors, Phys. Chem. Chem. Phys. **13**, 6223 (2011).

[17] Z. Wang, R. Hou, and A. Efremov, Directional fidelity of nanoscale motors and particles is limited by the 2nd law of thermodynamics—Via a universal equality, J. Chem. Phys. **139**, 035105 (2013).

[18] A. Yildiz, M. Tomishige, A. Gennerich, and R. D. Vale, Intramolecular strain coordinates kinesin stepping behavior along microtubules, Cell **134**, 1030 (2008).

[19] Z. Wang, Synergic mechanism and fabrication target for bipedal nanomotors, Proc. Natl. Acad. Sci. U.S.A. **104**, 17921 (2007).

[20] S. S. Rosenfeld, P. M. Fordyce, G. M. Jefferson, P. H. King, and S. M. Block, Stepping and stretching: How kinesin uses internal strain to walk processively, J. Biol. Chem. **278**, 18550 (2003).

[21] M. Liu, R. Hou, J. Cheng, I. Y. Loh, S. Sreelatha, J. N. Tey, J. Wei, and Z. Wang, Autonomous synergic control of nanomotors, ACS Nano **8**, 1792 (2014).

[22] B. E. K. Snodin, F. Randisi, M. Mosayebi, P. Šulc, J. S. Schreck, F. Romano, T. E. Ouldridge, R. Tsukanov, E. Nir, A. A. Louis, and J. P. K. Doye, Introducing improved structural properties and salt dependence into a coarse-grained model of DNA, J. Chem. Phys. **142**, 234901 (2015).

[23] E. F. Pettersen, T. D. Goddard, C. C. Huang, G. S. Couch, D. M. Greenblatt, E. C. Meng, and T. E. Ferrin, UCSF Chimera—A visualization system for exploratory research and analysis, J. Comput. Chem. **25**, 1605 (2004).

[24] G. M. Torrie and J. P. Valleau, Nonphysical sampling distributions in Monte Carlo free-energy estimation—Umbrella sampling, J. Comput. Phys. **23**, 187 (1977).

[25] L. Rovigatti, P. Šulc, I. Z. Reguly, and F. Romano, A comparison between parallelization approaches in molecular dynamics simulations on GPUs, J. Comput. Chem. **36**, 1 (2015).

[26] Z. Wang, M. Feng, W. Zheng, and D. Fan, Kinesin is an evolutionarily fine-tuned molecular ratchet-and-pawl device of decisively locked direction, Biophys. J. **93**, 3363 (2007).

[27] Y. Xu and Z. Wang, Comprehensive physical mechanism of two-headed biomotor myosin V, J. Chem. Phys. **131**, 245104 (2009).

[28] J. Cheng, S. Sreelatha, I. Y. Loh, M. H. Liu, and Z. Wang, A bioinspired design principle for DNA nanomotors: Mechanics-mediated symmetry breaking and experimental demonstration, Methods **67**, 227 (2014).
[29] R. Hou, I. Y. Loh, H. Li, and Z. Wang, Mechanical-Kinetic Modeling of a Molecular Walker from a Modular Design Principle, Phys. Rev. Applied **7**, 024020 (2017).
[30] C. S. Niman, M. J. Zuckermann, M. Balaz, J. O. Tegenfeldt, P. M. G. Curmi, N. R. Forde, and H. Linke, Fluidic switching in nanochannels for the control of Inchworm: A synthetic biomolecular motor with a power stroke, Nanoscale **6**, 15008 (2014).
[31] N. J. Kuwada, M. J. Zuckermann, E. H. C. Bromley, R. B. Sessions, P. M. G. Curmi, N. R. Forde, D. N. Woolfson, and H. Linke, Tuning the performance of an artificial protein motor, Phys. Rev. E **84**, 031922 (2011).
[32] D. Fan, W. Zheng, R. Hou, F. Li, and Z. Wang, Modeling motility of the kinesin dimer from molecular properties of individual monomers, Biochemistry **47**, 4733 (2008).
[33] W. Zheng, D. Fan, M. Feng, and Z. Wang, The intrinsic load-resisting capacity of kinesin, Phys. Biol. **6**, 036002 (2009).
[34] M. T. Downton, M. J. Zuckermann, E. M. Craig, M. Plischke, and H. Linke, Single-polymer Brownian motor: A simulation study, Phys. Rev. E **73**, 011909 (2006).
[35] D. Li, D. Fan, and Z. Wang, General mechanism for inchworm nanoscale track walkers: Analytical theory and realistic simulation, J. Chem. Phys. **126**, 245105 (2007).
[36] Z. Wang, Bioinspired laser-operated molecular locomotive, Phys. Rev. E **70**, 031903 (2004).
[37] X. Hu, J. Cheng, M. Liu, and Z. Wang (unpublished).
[38] K. Kawaguchi and S. Ishiwata, Temperature dependence of force, velocity, and processivity of single kinesin molecules, Biochem. Biophys. Res. Commun. **272**, 895 (2000).
[39] Z. Wang, G. R. Darling, and S. Holloway, The surface temperature dependence of the inelastic scattering and dissociation of hydrogen molecules from metal surfaces, J. Chem. Phys. **120**, 2923 (2004).
[40] S. R. W. Bellamy, S. E. Milsom, D. J. Scott, L. E. Daniels, G. G. Wilson, and S. E. Halford, Cleavage of individual DNA strands by the different subunits of the heterodimeric restriction endonuclease BbvCI, J. Mol. Biol. **348**, 641 (2005).

Correction: The inadvertent omission of a marker indicating Editors' Suggestion has been fixed.